Experimental Procedure

The chapter starts with a brief description of the deposition technique used for layer growth. Then the characterization tools used in this work are outlined. Particular emphasis is laid on the analysis of Raman and X-ray diffraction experiments which served as a standard tool for phase identification and structural characterization. Potential and limitations of the respective techniques with respect to thin film characterization are discussed.

2.1   System and Process Design

In general chalcopyrite thin films are deposited under non-stoichiometric conditions, where the chalcogen is offered at over-stoichiometric concentration. However final film compositions lie in the immediate vicinity of the Cu_2S-In_2S_3 pseudo-binary line (Figure 1.4). This is due to the high chalcogen vapor pressure at the deposition temperature ($> 400\,°C$) that hinders the incorporation of additional chalcogen atoms into the lattice. Depending on the deviation of molecularity Δm (Equation 1.1) of the elemental composition growth processes are divided into *Cu-poor* ($\Delta m < 0$) and *Cu-rich* ($\Delta m > 0$) ones. As discussed in Section 1.1.2 structural properties and the defect chemistry of the chalcopyrite phase are greatly influenced by the Δm parameter, independently of the specific film deposition method [33, 36, 38, 57]. Sophisticated coevaporation processes which are nowadays used for absorber layer preparation of the most efficient chalcopyrite thin film solar cells utilize this feature of the chalcopyrite system as they switch between the Cu-rich regime (to provoke large grain sizes and good structural properties) and the In-rich regime (to avoid secondary phases in the final layer) during film growth. Such processes are generally referred to as *two-stage* or *three-stage* processes.

Several deposition techniques have been reported for thin film growth of $CuInS_2$, i.e. single source evaporation [58], coevaporation from single sources [59], chemical vapor transport [60], spray pyrolysis [61], and reactive sputtering [62]. However, up to now device grade $CuInS_2$ material has only been achieved by either coevaporation of the elements or by two step processes were a precursor layer of metallic phases or binary sulfides is converted into a $CuInS_2$ film by a reactive annealing step in a sulfur containing atmosphere [33,

63, 64]. The growth process investigated in this work follows the latter approach, i.e. the sulfurization of metallic Cu-In and Cu-(In,Ga) stacks. In such a two step process, metal deposition and chalcogen incorporation are separate steps and the precursor composition mainly determines the molecularity. In the case of $CuInS_2$ thin film growth for photovoltaic applications the most efficient heterojunction solar cells have been achieved on the basis of Cu-rich prepared absorber layers [63, 65].

2.1.1   Process Design for $CuInS_2$ Thin Film Solar Cells

The general structure and the interface band line up of a chalcopyrite heterojunction solar cell was already discussed in Section 1.2.1. Figure 2.1 shows the schematic structure and a typical SEM cross section of a $CuInS_2$ solar cell prepared in this work. The structure consists of a metallic back contact (Mo), the p-type absorber layer ($CuInS_2$) and the n-type window layer (CdS + ZnO). The ZnO window layer is contacted by a Ni/Al grid. The process sequence is schematically depicted in Figure 2.2. In the following the preparation steps will be briefly outlined.
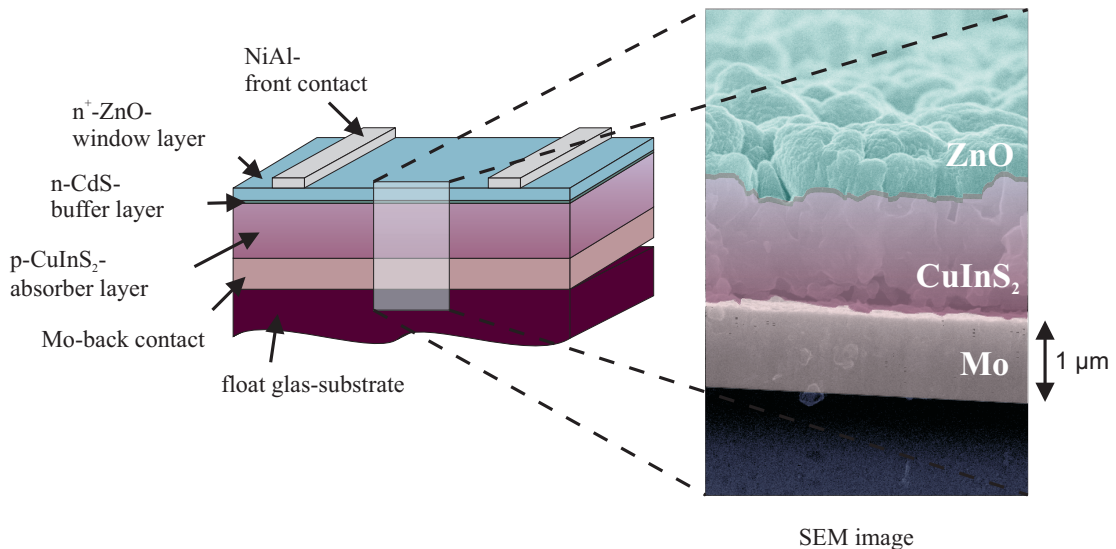

Figure 2.1: Schematic structure and SEM image of a cross-section of a $CuInS_2$ thin film solar cell showing the different layers which constitute the device. The SEM image has been shaded to highlight the different layers of the structure (marked CdS layer in the image is not to scale).

Back contact deposition   Conventional float glass substrates (thickness 2 mm) were used as sample substrates. The molybdenum back contact (layer thickness $1\,\mu m$) was deposited by e-gun evaporation onto heated substrates ($\approx 400\,°C$).
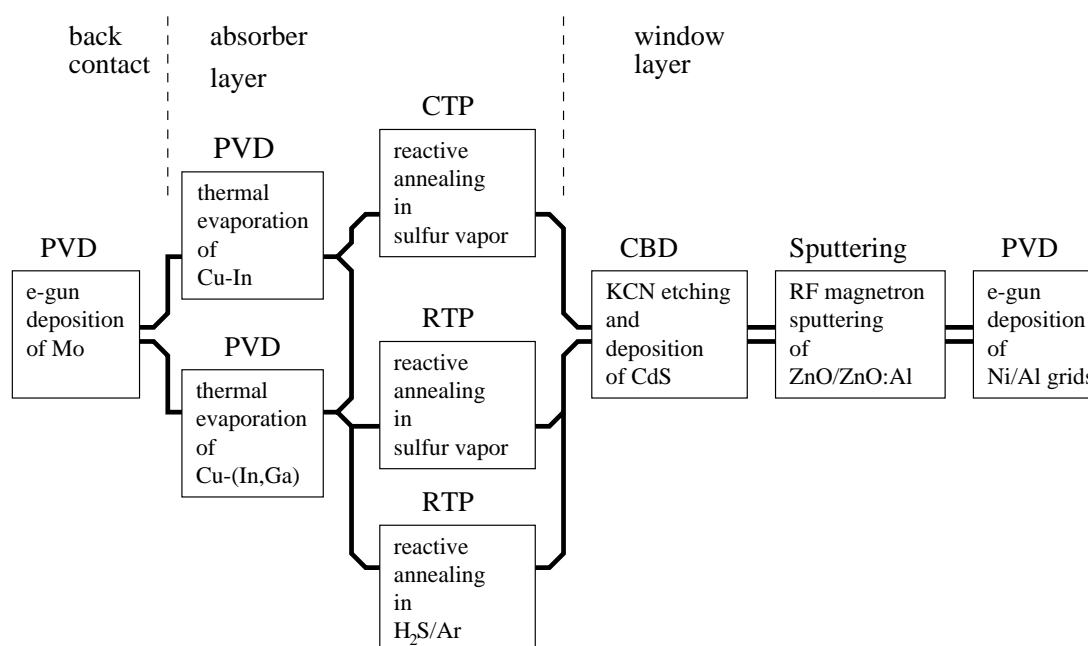
Figure 2.2: Process sequence used in this work for CuInS$_2$ thin film solar cell preparation. (PVD = physical vapor deposition, CTP = conventional thermal processing, RTP = rapid thermal processing, CBD = chemical bath deposition).

Precursor deposition Metal precursor layers were sequentially deposited by physical vapor deposition (PVD) from tungsten boats in a high-vacuum-system. No substrate heating was applied. Ultrapure pellets (99.9999 %) of Cu, In and Ga served as source materials. The deposited thickness was monitored in-situ by separate X-tal balances for each element. The atomic composition of the precursor was determined by adjusting the film thickness of each precursor layer. In addition the atomic ratios were controlled ex-situ by determining the amount of evaporated material. A precise determination of the precursor stoichiometry was realized by diluting the entire metal stack in a solution of concentrated HCl and concentrated HNO$_3$ at a ratio of 3:1 (*Königswasser*). Then the elemental concentrations in the solution were determined by *Inductively Coupled Plasma Atomic Emission Spectroscopy* (AES-ICP). Samples were stored in dry-air before further processing. The typical structure of a Cu-In-Ga precursor stack is depicted in Figure 2.3.

Reactive annealing The metallic precursor films were transformed to chalcopyrite absorber layers by reactive annealing or sulfurization* in an atmosphere containing either sulfur vapor S$_x$ or a H$_2$S/Ar mixture (5% H$_2$S). Three systems were available for this temper step, which mainly differed in the reactive atmosphere used for sulfurization and in the substrate heater design.

---

*The terms reactive annealing and sulfurization will be used equally in the text. Both terms refer to the transformation of a precursors into a chalcopyrite in a sulfur containing atmosphere.

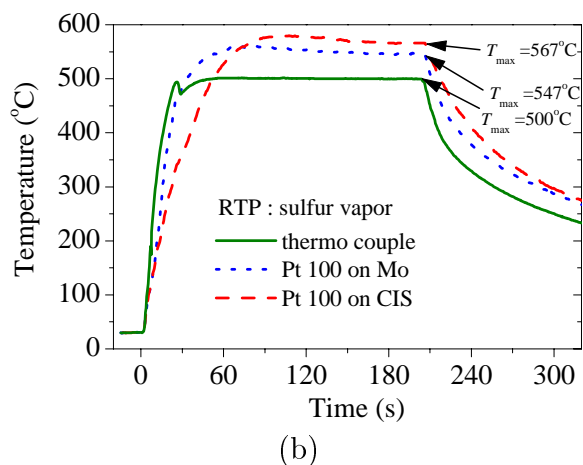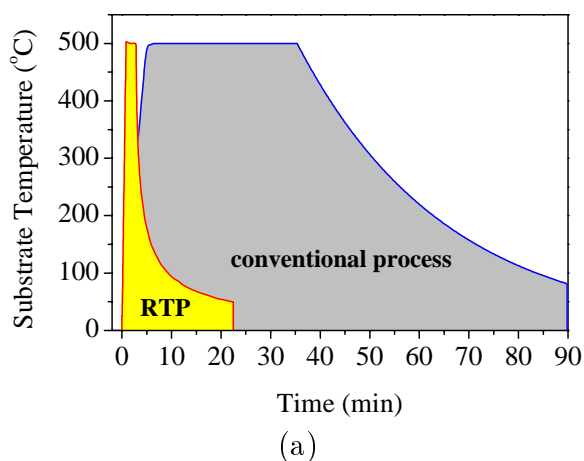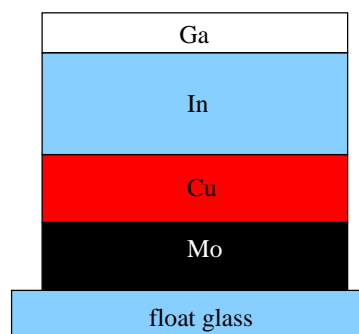Figure 2.3: Structure of metallic Cu-In-Ga stack (precursor).

(a)

(b)

Figure 2.4: (a) Characteristic temperature profile of a RTP sulfurization process and a conventional process. (b) Temperature profile of RTP annealing step (S_x system) as measured by a thermo couple, a platinum resistor at the Mo back layer and a platinum resistor at the CuInS$_2$ layer (redrawn from [66]).

1.) Conventional Thermal Processing (CTP): In this system a reactive atmosphere was established from a source containing a liquid sulfur bath at $T = 200\,^{\circ}\text{C}$. Process pressure was around $10^{-3}\,\text{mbar}$ during sulfurization. Substrates were heated by an conventional resistor heater to temperatures around $500\,^{\circ}\text{C}$. Annealing times at $500\,^{\circ}\text{C}$ were between 15 to 30 minutes.

2.) Rapid Thermal Processing (RTP): Two RTP-systems were also used for precursor sulfurization. Due to the low thermal mass of such a system (substrates are heated by a UV-lamp field) very short heat up and cool down ramps can be realized. Therefore the RTP systems were also used for quenching experiments which allowed for an ex-situ investigation of the film growth behavior (Chapter 3). Sulfur was supplied either by putting sulfur powder next to the substrate which evaporates once the substrates are heated or by a H_2S/Ar gas flow. Process pressure was around $1\,\text{mbar}$ in the sulfur vapor system and $500\,\text{mbar}$ in the H_2S/Ar system. Typical annealing times were as short as 5 minutes. Figure 2.4 (a) shows characteristic temperature profiles of a RTP sulfurization process and a conventional process. Experimental values for the substrate temperature were found to vary up to $\approx 50\,\text{K}$ depending on the specific sensor and/or on the probing point at the sample or sample holder (Figure 2.4). Substrate temperature values given in this work are always as read on the meter, thus they might be the subject to a substantial absolute error. However, relative changes in temperature were found to be very reproducible in all systems. Since different devices were used for temperature control in the individual systems substrate temperature values can not be compared directly between the different systems.

Window layer deposition   The window layer consist of n-type CdS buffer layer of about $50\,\text{nm}$ thickness, a n-type ZnO layer of $100\,\text{nm}$ thickness, and a n^+-type ZnO:Al layer. Before the window layers are deposited the secondary CuS phase which forms during reactive annealing is removed by selective etching in a KCN solution. The CdS buffer layer is deposited immediately after KCN etching by chemical bath deposition at a substrate temperature of $60\,^{\circ}\text{C}$. The ZnO layers are sequentially deposited by RF magnetron sputtering from a ZnO and a ZnO:Al target. Ni/Al front grids are deposited by e-gun evaporation.

2.2   Structural Characterization

Several characterization techniques have been employed for sample analysis, i.e. secondary neutral mass spectrometry (elemental depth profiling), micro-Raman spectroscopy and X-ray diffraction (phase analysis, structural analysis) and inductively coupled plasma atomic emission spectroscopy (atomic sample composition). Potential advantages and limitations of these techniques with respect to thin film analysis will be discussed in the following. Information about film roughness and morphological grain size were obtained from scanning electron microscopy images (SEM). In addition a small number samples was forwarded to transmission electron microscopy (TEM).

2.2.1   Depth Profiling

In order to determine the elemental composition and depth distribution of $Cu(In_{1-x}Ga_x)S_2$ thin films secondary neutral atom mass spectrometry (SNMS) was used. SNMS is very similar to the widely used secondary ion mass spectrometry (SIMS), but here neutral atoms, which are ionized separately, are used for mass spectrometry. Mass analysis in a SIMS measurement is based on the fact that a certain fraction (less than 1 % [67]) of the sputtered species is ionized. This fraction, i.e. the ionization yield, differs for different elements and compounds and is also sensitive to the structural properties of the sample. As long as the yield is known the final result can be corrected, however, especially in polycrystalline samples the ionization yield might well be influenced by local variations of the micro-structure in the vicinity of the sputtered atom (matrix effect), by oxidized surfaces and by changing surface compositions [68]. In SNMS, the uncertainty introduced by these effects is circumvent by separating the sputtering and the ionizing process. Only neutral atoms, which are ionized in a separate ionizer are used for analysis. The sputtering yield, i.e. the fraction of eroded atoms per incident ion flux, is, in general, also a function of the above mention sample specific parameters. However, after some ten nanometers surface depletion and sputtering yield of each atomic specimen in the sample will approach an dynamic equilibrium, so that the composition of the sputtered secondary atoms reflects the sample composition; in other words the sputtering process "self adjusts". In a polycrystalline sample this might not be fully true as the sputtering yield can vary across the sample volume, in particular if the sample exhibits phase boundaries or large changes in structural properties (grain size, defect density etc.). When analyzing the experimental output it is difficult to differentiate such changes in sputtering yield from pure compositional changes. Furthermore Cu-chalcopyrites haven proven to be very susceptible to roughness development during Ar-sputtering [69]. Similar effects are known for indium containing III-V compounds. In the latter case the effect has been ascribed to indium enrichment at the surface, which occurs due to the preferential sputtering of the V-compound and surface diffusion of indium [70]. As a result of the different etch rates of indium and the surrounding In-V compound, the In-islands act as a shield for the underly-

ing layer leading to an increase in surface roughness with ongoing sputtering [70]. Sample rotation [69] and reactive sputtering with N_2 [70] have been suggested to overcome this problem. In the latter case the suppression of In-segregation was tentatively assigned to Indium nitride formation at the surface, which has roughly the same sputter yield as the bulk material. Furthermore it is believed to protect the underlying regions from sputter-damage (important when using sample for PL or Raman) [71]. Another source of error is radiation-enhanced diffusion [68]. Sputter induced defects at the surface can migrate into the bulk, thereby changing the original composition of the sample. According to Eicke [72] Cu depth profiles of $Cu(In_{1-x}Ga_x)Se_2$ were found to be very sensitive to sputtering conditions, which was related to the high mobility found for Cu in chalcopyrite lattices [73]. By significantly reducing the substrate temperature to e. g. liquid nitrogen temperature such effects can be reduced [67]. Surface roughness might be another problem, which can have detrimental effects on the depth resolution of the measurement, since the sputtering yield depends on the angle between the incident ion beam and the sample surface. As a rule of thumb in many cases the yield is greatest at an angle of 45°. That means, assuming normal incidence of the sputter species, a tilted surfaces of a crystalline grain will sputter off faster than a surface parallel to the substrate. Hence, surface roughness is preserved or even enhanced by the etching process. Again, the effect can be significantly reduced by rotating the sample during the process. However, although some of the discussed effects can be minimized under certain experimental conditions, they have to be considered when analyzing elemental depth profiles from SIMS or SNMS experiments.

All SNMS measurements reported in this work have been carried out in a *LHS10* system with a *SSM 200* (electron beam SNMS) at the Zentrum für Sonnenenergie- und Wasserstoff-Forschung Stuttgart (ZSW). The SNMS profiles were collected under the following conditions. An focused Ar^+ beam of $E = 5\,keV$ and $I \approx 1\,\mu A$ under an incident angle of 60° (with respect to the sample normal) was used for sputtering. Two different sputter modes have been used: 1. stationary samples which were cooled down to liquid nitrogen temperature, and 2. rotated samples at room temperature. The sputtered species were ionized by means of a cross-beam electron source ($E = (50\text{--}80)\,keV$), whereby a electronic lens system assured that only neutral atoms could reach the ionizer. Then the ionized atoms were passed through a quadrupol mass spectrometer and finally detected by a Cu-Be-dynode. Secondary electrons emitted from the dyode were amplified by a photomultiplier and a pre-amplifier to a recordable signal. The raw data in counts per seconds was converted to concentration profiles by using experimentally determined sensitivity factors. These factors where based on system calibrations performed at $Cu(Ga,In)(S,Se)_2$ single crystals and thin films of known composition.
There was a significant variation in total sputter rate as a function of sample composition and a drastic drop in sputter rate once the Mo-back contact layer was reached. Figure 2.5 shows the sum of the Cu, In, Ga, and S count rate, corrected by the respective sensitivity factor. The effect of film morphology and composition onto the sputter rate can clearly be seen in the figure. Without sample rotation (subfigure (a.)) films with larger grains sputter off faster and the rate varies quite significantly over time. The effect is substan-
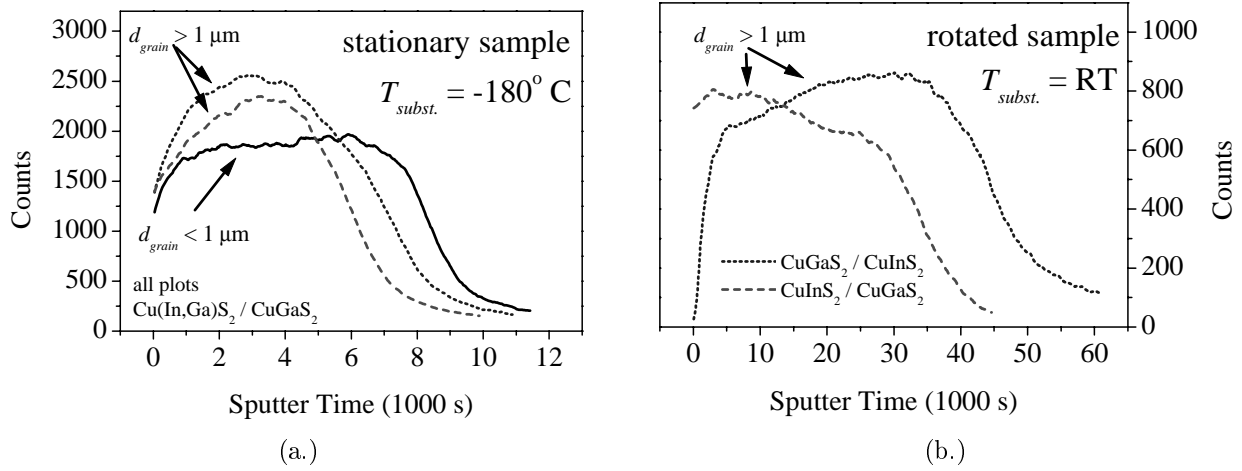
Figure 2.5: Sum of corrected count rate of Cu, In, Ga, and S versus sputter time indicating sample dependent variations in sputter rate caused by (a) the grain sizes of the film, and (b) by the stacking sequence of different phase in the film.

tially reduced, if the samples is rotated during sputtering (subfigure (b.)). Since the data in subfigure (b) was collected at $CuInS_2/CuGaS_2$ bilayers of similar grain size but different stacking sequence the changes in total sputter rate have to be assigned to the changing composition with depth. The plots indicate a higher sputter rate for polycrystalline $CuInS_2$ when compared to $CuGaS_2$. The sputter rate of $CuGaS_2$ seems to be by one fifth smaller compared to $CuInS_2$.

2.2.2   Micro-Raman Spectroscopy

Raman spectroscopy has become a widely used method for the analysis of semiconductor layers. Its non-destructive nature, its high sensitivity for very thin films, its variable information depth and the fast evolution of sophisticated equipment in recent years have lead to the wide-spread application of Raman spectroscopy. The so-called micro-Raman spectroscopy, which allows measurements of lateral resolution in the micro meter range, has further widened the field of applications.
In principle, the method is based on inelastic scattering of photons at lattice vibrational modes, e.g. at phonons. By evaluating the phonon frequencies, and the intensities, half widths, and shapes of lines in the Raman spectra the specific lattice dynamics of the sample can be investigated. This information can than be related to structural properties such as identification of materials and compounds, composition of mixed compounds, layer orientation, stress and crystalline perfection. In addition resonance Raman spectroscopy can be used to investigate the critical points in the electronic energy bands. Section 2.2.2.1 will first outline some fundamentals of Raman scattering. Then dominant lattice vibrational modes in Cu-chalcopyrites will be presented in section 2.2.2.2. Subsequently, the deter-

mination of composition of mixed compounds, such as $Cu(In_{1-x}Ga_x)S_2$, will be discussed. Finally, a short description of the experimental set up is given in section 2.2.2.3.

2.2.2.1   Principles of Raman

Raman spectroscopy observes inelastic light scattering processes where energy of an incident photon of energy $\hbar\omega_i$ is transfered to the sample and to a scattered photon of slightly different energy $\hbar\omega_s$. The energy transfered to to the sample corresponds to the energy $\hbar\Omega_j$ of, e.g. a phonon j. Since the frequency of the incident light ω_i can be well defined by using a laser the energy Ω_j of the phonon involved in the scattering process can be obtained by analyzing the peak frequencies ω_s of the scattered light. Energy as well as quasi-momentum have to be conserved in the process:

$$\hbar\omega_s = \hbar\omega_i \pm \hbar\Omega_j \quad ; \mathbf{K}_s = \mathbf{K}_i \pm \mathbf{q}_j \, , \tag{2.1}$$

where $\mathbf{K}_{i,s}$ refers to the photon wave vectors and $\mathbf{q}_j$ to the wave vector of the phonon. The $\pm$ sign in Equation (2.1) results from the fact that in the scattering process a phonon is either generated (Stokes process) of annihilated (Anti-Stokes process). In most experiments only Stokes processes are investigated. As a result of the conversation of energy and momentum only certain combinations of energy and momentum can be transfered to the sample. Typical $|\mathbf{q}_j|$ values lie in the range of $10^6\,\mathrm{cm}^{-1}$, hence only phonons in the immediate vicinity of the center of the Brillouin zone can be involved in a Raman process.

In the scattering process the interaction between the photon and the phonon acts via electronic inter-band transitions (indirect process). According to [74] Raman light scattering can be described in a microscopic quantum mechanical time-dependent perturbation theory. Here the photon-electron and the electron-lattice interaction is described by three electronic transitions:
1- the absorption of a photon leading to an electronic transition from a ground state $|0\rangle$ to an excited state $|e\rangle$.
2- the electron-lattice interaction, i.e. the electronic transition from a state $|e\rangle$ to a state $|e'\rangle$ which involves the creation or annihilation of a phonon $\hbar\Omega$.
3- the recombination of the electron-hole pair under emission of a photon $\hbar\omega_s$ which corresponds to the transition $|e'\rangle$ to $|0\rangle$.
In this picture the transition $|e\rangle \rightarrow |e'\rangle$ corresponds to transitions between intermediate states in the same band caused by a phonon-induced energy shift of the band itself (intra-band electron-phonon interaction). Inter-band electron-phonon interactions are also possible, however the scattering efficiency is much smaller. Since the energy conservation needs only to be full-filled for the process as a whole the electron-hole pairs states involved in the process are virtual states and must not necessarily coincide with the real electronic band structure. If, however, transition energies correspond to real states in the band structure the transition probabilities drastically increase leading to much higher Raman scattering cross sections for excitation energies close to e.g. band gap energies (resonant Raman scattering).
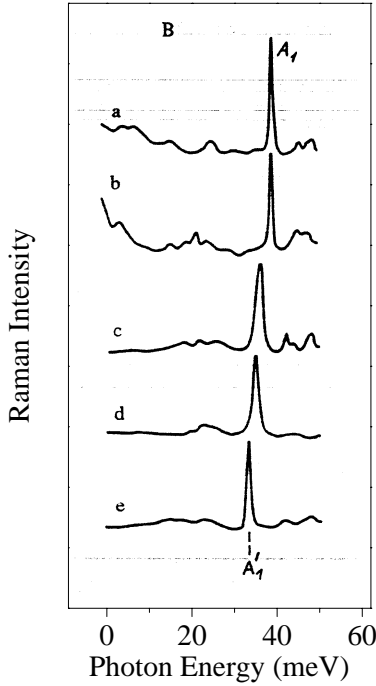
2.2.2.2 Raman at Cu-chalcopyrites

Figure 2.6: Spectral Position of Raman A_1 mode as a function of composition in $Cu(In_{1-x}Ga_x)S_2$, $x = 1$ (a), $x = 0.86$ (b), $x = 0.5$ (c), $x = 0.3$ (d), $x = 0$ (e) [75].

One of the first reports of Raman spectroscopy studies at a chalcopyrite semiconductor ($ZiSiP_2$) was published by Kaminow et al. [76]. Later Koschel and Bettini [77] presented lattice dynamical calculations of some chalcopyrite compounds and were able to predict some so far unobserved modes. A detailed report on experimental results of the Raman spectra of $CuInSe_2$ was published by Tanino et al. [78]. Meanwhile there is a considerable number of publications regarding Raman spectroscopy of Cu-chalcopyrites single crystal and thin film specimen. A concise review covering experimental results as well as lattice dynamical calculation of chalcopyrite compounds has been given recently in a series of publications by Ohrendorf and Haeuseler [79–81].

The chalcopyrite-structure has four formula units in the tetragonal unit cell. The primitive cell contains two formula units, i.e. eight atoms per unit cell. Therefore 24 vibrational modes (3 acoustic, 21 optical) can be expected. In order to detect a phonon in a Raman experiment the phonon must obey certain necessary conditions (Selection Rules), which are based on symmetry considerations derived form the crystal structure under investigation. If the phonon can be observed in Raman it is also called Raman-active. According to a group theoretical treatment by Kaminow et.al. [76] the following irreducible representation of the optical phonons at the zone center results

$$\Gamma = A_1(Ra) + A_2 + 3B_1(Ra) + 3B_2(IR, Ra) + 6E(IR, Ra). \qquad (2.2)$$

Ra and IR in parentheses stands for Raman and Infra-red active respectively. In the case of non-resonant scattering the Raman component corresponding to the A_1 mode is much stronger than any other. Therefore the analysis of Raman spectra of $CuInS_2$ and $Cu(In_{1-x}Ga_x)S_2$ thin films will be based mainly on the A_1 phonon line. The A_1 mode is caused by the vibration of two pairs of anions, with one vibrating in the direction of the a-axis and the other in the direction of the b-axis.

Since optical phonons are a fairly unique fingerprint of a certain material, phase identification by Raman is a more or less straightforward procedure. Furthermore variations of the composition of a compound can well be resolved from the energies of the phonon modes. The relationship between the vibrational dynamics of a mixed compound and its composition (or stoichiometry) can be classified into three types: i.e. one-mode, two-mode,

and three-mode behavior. In the one-mode case the constituent compounds have the same phonon modes and their frequencies varies approximately linearly with composition between the respective end point values. In the two-mode case, the intermixing materials exhibit separate phonon modes, which vary characteristically, in general not linearly, with composition. At intermediate composition modes of both materials will be observed. In the three-mode case additional modes, only characteristic for the mixed compound, appear beside the modes of the endpoint materials.

The vibrational system of solid solutions in Cu-chalcopyrites transforms in the two-mode manner in the case of anion substitution and in the one-mode manner in the case of cation substitution [75,82]. Correspondingly the $CuInS_2$-$CuGaS_2$ system shows one-mode or uni-modal behavior. This was experimentally confirmed by Agkyan et al. [75] who found an continuous shift in the A_1 peak position with composition x. Furthermore they found that in the range of $0.3 < x < 0.8$ the mode was strongly broadened (Figure 2.6). As outlined above the A_1 is caused by the vibrational motion of the anion lattice. The shift of its spectral position is mainly due to the slightly altered Ga-S binding force with respect to In-S and the smaller atomic weight of Ga. The shift between $CuInS_2$ and $CuGaS_2$ is about $18\,cm^{-1}$ ($36\,meV$ to $39\,meV$ in Figure 2.6). Taking into account the typical experimental resolution limit of 1–$2\,cm^{-1}$ the composition can be determined to an accuracy of about $5\,\%$. This might seem to be a moderate value compared to methods such as XRD, which, in general, give results of much higher accuracy based on precise lattice constant determinations. Nevertheless the determination of composition by means of Raman offers a number of advantages. Particularly in thin film analysis an optical method, such as Raman, might be more suitable as the required minimum layer thickness is lower than for X-ray diffraction. Furthermore in the case of $CuInS_2$ the penetration depths of the laser light used for excitation is only $100\,nm$ ($1/20$ of the typical absorber layer thickness), a fact that offers the possibility of depth-resolved measurement, when the Raman measurement is combined with ion-etching methods. In micro-Raman mode the high lateral resolution allows to perform homogeneity studies of composition in the micro meter range across a samples surface.

Besides the identification of phases or the determination of compositions Raman spectrometry provides valuable information on the degree of crystallinity of a sample. Real crystal structures are always the subject of impurities and dislocations. These effects may be responsible for the non-conversation of momentum in the scattering process which is experimentally reflected by a corresponding broadening of the spectral lines. The line shape of phonon peaks observed in a Raman spectrum can thus be used to characterize the degree of disorder in a solid. The lifting of momentum conservation with structural disorder can even lead to acoustical phonons contributing to the Raman signal which will lead to a very broad "background" in the spectra in the vicinity of the excitation laser line.

2.2.2.3   Raman - Experimental

All micro-Raman spectra reported in this work were measured at the University of Barcelona. The spectra were taken by means of a *Jobin-Yvon T64000* spectrometer coupled with an *Olympus* metallographic microscope. The obtained spot size on the sample was slightly submicronic (objective: x100, NA = 0.95). All spectra were recorded in backscattering configuration. The sampling volume of a Raman measurement is limited on one hand by the spot size on the other hand by the penetration depth of the laser light used for excitation. In our case the green line of an Ar^+ laser ($\lambda = 514.5\,nm$) was used which corresponds to a sampling depth of about 100 nm in $CuInS_2$; less than one twentieth of the usual total absorber thickness.

Depth-dependent information on film structure could be gained by repeatedly sputtering (Ar^+) the sample and performing Raman measurements in between. A *PHI 670 Scanning Auger Nanoprobe System* was used for sputtering. Simultaneously the atomic composition was determined by *Auger Electron Spectroscopy* (AES) between successive sputter steps. A 10 nA current of 10 keV electrons was used for AES. The ion energy for sputtering was 2 keV. The ion current was fixed at a nominal value of $50\,\mu A$ for all sputter steps. Reference Raman measurements at $CuInS_2$ single crystals did not reveal any significant sputter related damage under the described experimental conditions.

2.2.3   X-ray Diffraction

XRD measurements served as a standard tool for phase identification throughout this work. The method was also employed in order to resolve Ga-induced effects on structural parameters such as lattice constants, anion displacement, and tetragonal distortion by analyzing the peak position and integral intensity of selective reflections. XRD measurements were performed using a *Brucker D8* diffractometer. This section starts with a brief overview of fundamental aspects which determine the intensity of a X-ray reflection. The influence of instrumental parameters as well as sample related parameters onto line shape and position of a XRD reflection will be briefly discussed. Then numerical calculations of XRD-spectra of $CuInS_2$ thin film samples will be outlined. Furthermore XRD-spectra of films with gradients in lattice constant will be discussed. Correction factors necessary when analyzing thin film samples are discussed in Appendix A.3.

2.2.3.1   The scattered intensity

The scattered intensity in a X-ray diffraction experiment can well be described in terms of classical theory of scattering of X-rays by electrons (kinematical theory). When electromagnetic radiation falls on an atom, or more precisely on the electronic sphere of the atom, two processes may occur: (1) the radiation may be absorbed with an ejection of electrons

from the atom, or (2) the radiation may be scattered. In X-ray diffraction only the latter process is important. The scattered radiation, which spreads out in all directions from the atom has the same frequency as the primary radiation (elastic scattering). In high resolution X-ray diffraction the kinematical approach, which treats the electro magnetic field strength as a planar wave, fails to predict the experimentally observed intensities and a more fundamental, dynamical theory, becomes necessary. The following outline is restricted to the kinematical case.

In X-ray diffraction the scattered intensity is caused by interference between waves scattered from the different atomic sites within the crystal. When treating the scattering process as a *classical* reflection of X-rays at a set of periodically spaced lattice planes the common *Bragg Law* can be derived, which in vector form is given by

$$\frac{\mathbf{s} - \mathbf{s}_0}{\lambda} = \mathbf{G}_{\mathbf{hkl}} \, , \tag{2.3}$$

$$\text{where} \quad |\mathbf{G}_{hkl}| = \frac{1}{d_{hkl}} \, , \quad |\frac{\mathbf{s} - \mathbf{s}_0}{\lambda}| = \frac{2\sin\Theta}{\lambda} \, .$$

Here $\mathbf{s}_0$ and $\mathbf{s}$ are unit vectors in the directions of the primary and diffracted beams $\mathbf{k}_0$ and $\mathbf{k}$, $\mathbf{G}_{hkl}$ is called the scattering vector, d_{hkl} is the distance between equivalent lattice planes, and Θ denotes the angle between the lattice planes and the incident or the diffracted beam. The indices (hkl) are the Miller indices of the set of lattice planes which causes the reflection. In the case of an orthogonal crystal structure with lattice constants a, b, and c the lattice plane spacing d_{hkl} is given by

$$\frac{1}{d_{hkl}^2} = \frac{h^2}{a^2} + \frac{k^2}{b^2} + \frac{l^2}{c^2} \, . \tag{2.4}$$

The Bragg-law describes the angle under which a XRD-reflection will occur in experiment. As mentioned above the scattered intensity is caused by interference between waves scattered from the different atomic sites within the unit cell. The total scattered intensity is then obtained by 1.- summing over the scattered intensity of each atom α in the crystal unit cell, usually described in terms of a atomic scattering factor f_α, multiplied by a phase factor which accounts for the different positions $\mathbf{r}_\alpha$ in the unit cell and 2.- summing over all unit cells N in the sample,

$$I(\mathbf{G}_{\mathbf{hkl}}) \propto K \frac{I_0}{r^2} N^2 |F_{hkl}|^2 \text{ where, } F_{hkl} = \sum_\alpha f_\alpha e^{-\mathrm{i}\,\mathbf{G}_{hkl}\cdot\mathbf{r}_\alpha} \, . \tag{2.5}$$

F_{hkl} is called structure factor. I_0 stands for the initial intensity and r for the distance between sample and detector. The factor K has been introduced to account for corrections due to sample geometry and experimental set up. Several contribution to the correction factor K are discussed in Appendix A.3. Equation (2.5) shows that all sample dependent information regarding the intensity of a reflection (hkl) is contained in F_{hkl}, whereas all other terms in the equation are sample independent. The atomic position $\mathbf{r}_\alpha$ in the unit cell

is usually expressed in terms of components along the basis vectors of the lattice $\mathbf{a}_1, \mathbf{a}_2, \mathbf{a}_3$ by means of fractional coordinates $u, v, w \in [0 \dots 1]$. The structure factor may then be written

$$F_{hkl} = \sum_{\alpha} f_{\alpha} \exp[-2\pi i(hu_{\alpha} + kv_{\alpha} + lw_{\alpha})] \,. \tag{2.6}$$

In brief, the shape and dimension of a crystal unit cell can be deduced from the position of XRD-reflections, the "content" of the cell can be determined from the intensity.

2.2.3.2   Peak profile analysis

In an experiment the overall intensity of a XRD-reflection will be spread out over a finite angular range. The width of this range, i.e. the full width at half maximum (FWHM) of the XRD reflection, is determined by several independent effects. The final line profile of the reflection can be considered as a convolution product of

- the emission profile of the source

- specimen aberrations due to finite grain size, strain, and defect concentrations, as well as absorption in the sample, finite sample thickness, and tilt of the sample

- an instrument component which determines the angular resolution of the experimental set up

With current diffractometers instrument broadening can be minimized to a level, so that, assuming a perfect sample, the emission profile becomes a significant part of the total observed line profile. The emission profile of the Cu-K$_{\alpha}$ radiation mainly consists of two contributions K$_{\alpha 1}$ and K$_{\alpha 2}$. Due to the fine-structure of the underlying electronic transitions the emission lines are slightly asymmetric. The profile can be sufficiently approximated by means of two Lorentz-profiles [83]. Since the incident radiation is never exactly monochromatic the half width of a reflection is broadened (dispersion). In XRD spectra collected in this work the peak splitting due to the emission line doublet K$_{\alpha 1}$ and K$_{\alpha 2}$ could be well resolved. However, the peak shapes were either determined by instrumental or by sample related broadening. Sample broadening arises mainly from the fact that the scattered intensity is due to a coherent superposition of scattered X-ray waves. In practice only a finite volume of the crystal will lead to coherent scattering. Effects which determine this volume might be crystallographic defects (point defects, dislocations), grain boundaries, or the finite thickness of the sample itself. According to Scherrer [84] the finite grain size d in a polycrystalline sample leads to a broadened intensity profile $I(\mathbf{G})$ of half width

$$\Delta|\mathbf{G}| = 0.9 \cdot 2\pi/d \,. \tag{2.7}$$

The corresponding line profile can be described by a Lorentz-profile. The FWHM$_{gs}$ of such a grain-size broadened profile was given by Cheary [85] as

$$\mathrm{FWHM}_{gs} \propto \frac{1}{\cos \Theta d} \,, \tag{2.8}$$

where $[d]$ = nm. In the case of polycrystalline samples with grain sizes d in the submicron range the above relation allows for a determination of d by evaluating the FWHM of the line profile of the XRD reflection, presuming instrumental broadening can be neglected or has been corrected for.
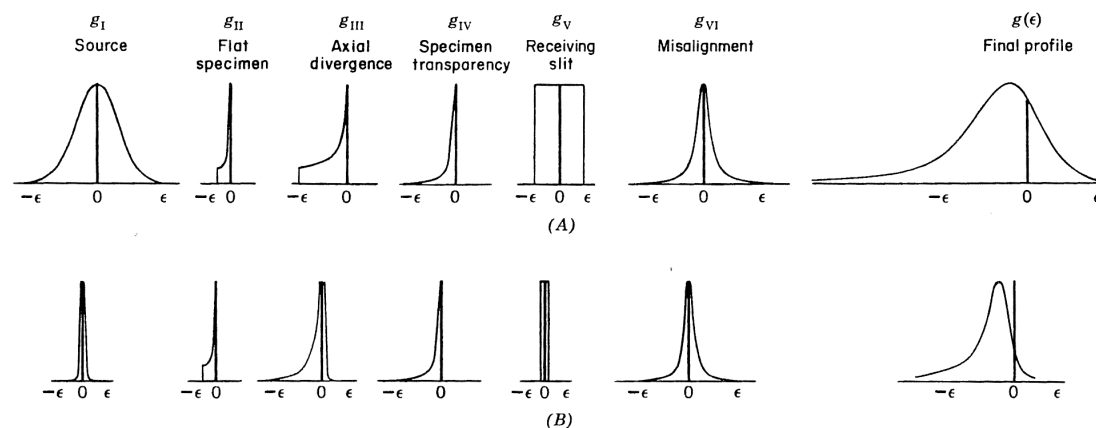

Figure 2.7: The six instrumental weight functions for a (A) low-resolution and (B) high resolution diffractometer [86].

A detailed overview about effects leading to instrumental broadening can be found in [87]. Effects, which affect the shape, symmetry and position of a reflection and which are introduced by the geometry of the experimental set up include [88]:

- flat specimen error

- axial divergence or brush effect

- specimen transparency

- generator focus, effects of apertures, and misalignment

Each individual effect leads to a characteristic deviation of the peak profile. Figure 2.7 plots the experimental weight functions for the six most important experimental errors for a low resolution and a high resolution diffractometer [86]. A convolution of all effects results in the final profile . Among them the flat specimen error and the axial divergence turned out to be the most important ones in measurements of this work. The flat specimen error arises from the fact that a flat sample lies tangential at the circle of focus (see Figure 2.9). This leads to asymmetric broadening and a shift of the peak to lower 2Θ values. The error can be reduced by means of apertures. The fact that the mean scattering volume is located below the sample surface causes an additional peak shift due to deviations from the ideal beam geometry. The magnitude of this shift strongly depends on the absorption coefficient of the sample. However, for $\mu > 250\,\mathrm{cm}^{-1}$, as in $CuInS_2$, it turns out to be below $\Delta\Theta = 0.01°$ [89]. The divergence of the incident and the diffracted beam in the

plane normal to the circle of focus leads to the so-called *Brush effect*. Numerically this effect causes the largest asymmetrical broadening. It also leads to a Θ-dependent shift (to smaller values for $\Theta < 90°$). Again, the effect can be reduced by additional apertures in the beam path (Soller-Blenden).

The focus of the primary beam generated in the X-ray tube is very sensitive to the operating conditions of the tube. Therefore scans were always performed at the same generator voltage and current; the same values which were also used for system calibration. Changes of the line shape due to the apertures in the beam path were negligible in our set up, when compared to the effects discussed above.

Misalignment of the set up can lead to significant shifts in the measured angular position of the XRD reflection. Here the biggest source of error will be introduced by a displacement of the sample surface with respect to the ideal position of the circle of focus. As is depicted in Figure 2.8 the peak shift is given by

$$\frac{2S \cos \Theta}{R} = \tan \Delta 2\Theta \approx \Delta 2\Theta \,, \quad \Theta \ll 1 \,, \tag{2.9}$$

where S is the sample displacement and R is the radius of the goniometer. The corresponding peak shift for an assumed misalignment of the sample surface of $50\,\mu$m are plotted in Figure 2.8. In the range of low Θ values sample displacement was found to be the biggest source for errors in peak position.
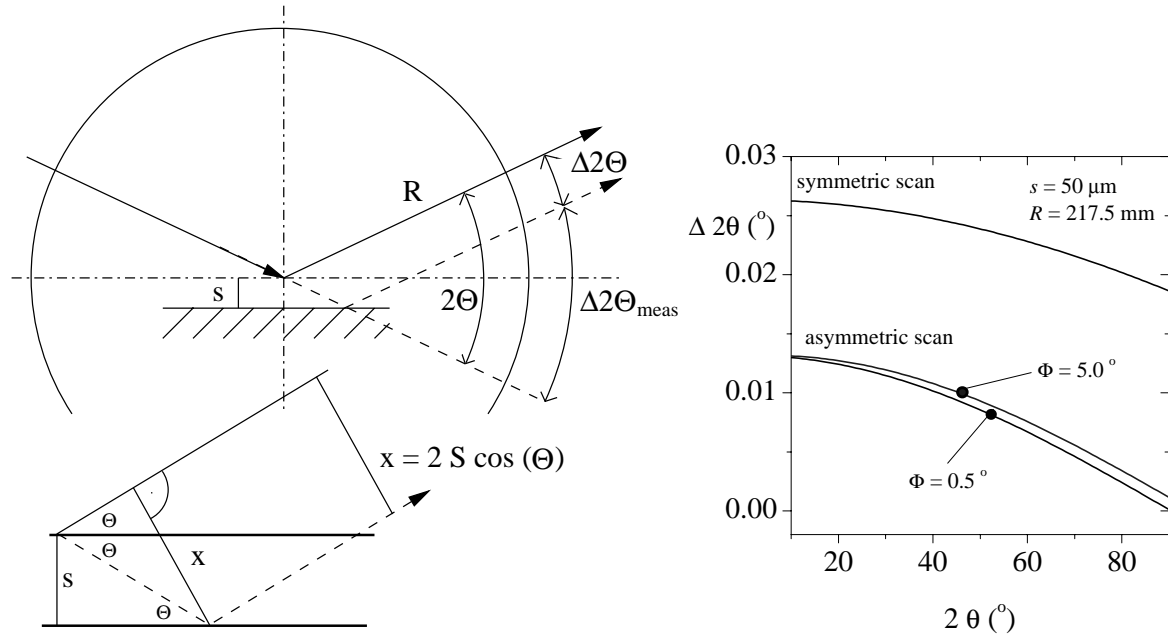

Figure 2.8: Systematic peak shift due to misalignment of sample.

In general measured patterns from an X-ray powder diffractometer cannot be fitted by a simple analytical function such as a pure Gauss or Lorentz profile. Several analytical peak

shape functions had been proposed. Best results were obtained by using pseudo-Voigt or Pearson-VII functions. These functions are not only characterized by peak position, intensity and full-width-at-half-maximum but also by an additional parameter n that defines the fraction of Lorentzian to Gaussian character of the profile. Kern [88] has compared several peak shape function for the precise determination of the peak position and obtained best result when using a Pearson-VII function given by

$$I_{i,k} = \frac{\Gamma(n)}{\Gamma(n-0.5)} \frac{(2^{1/n}-1)}{\pi} \frac{2}{FWHM_k} \left[1 + 4(2^{1/n}-1) \left(\frac{\Delta 2\Theta_{i,k}}{FWHM_k} \right)^2 \right]^{-n}, \qquad (2.10)$$

where $\Delta 2\Theta_{i,k} = 2\Theta_i - 2\Theta_k$. $\Gamma(n)$ is the gamma function. When $n = 1$ the Pearson-VII becomes a Lorentzian and when $n \to \infty$ it becomes a Gaussian.

2.2.3.3   XRD-Experimental

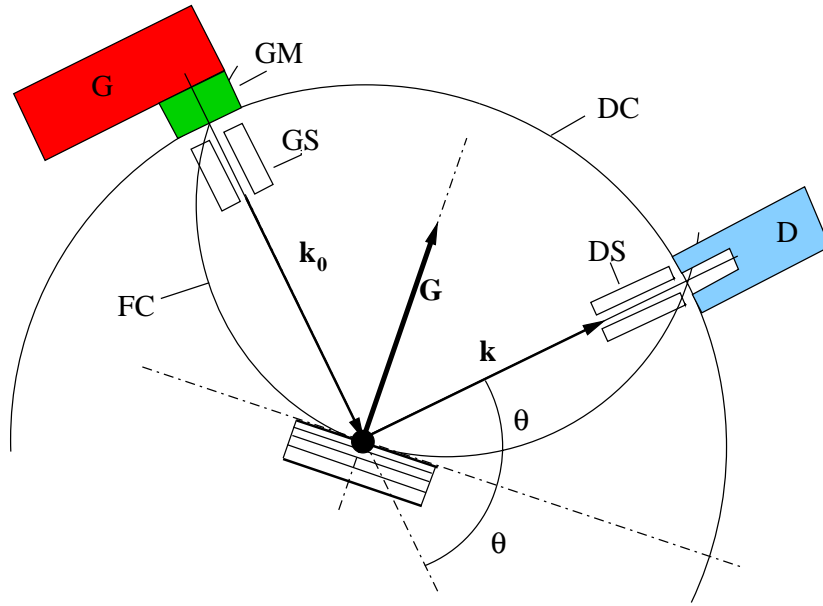All XRD-scans where collected in Bragg-Bretano geometry (Figure 2.9). The Cu-K$_\alpha$ dou-

Figure 2.9: Bragg-Bretano geometry used in the *Brucker D8* diffractometer. G - generator, D - detector, GM - Goebel Mirror, GS - generator Soller aperture, DS - detector Soller aperture, FC - focusing circle, DC - detector circle.

blet from a Cu-anode (generator settings $E = 40\,\mathrm{keV}$, $I = 40\,\mathrm{mA}$) was used as incident radiation. For better collimation of the incident beam a *Goebbel-mirror* was attached to the exit slit of the generator. The Goebbel-mirror also removed Cu-K$_\beta$ radiation from the incident beam. A szintilization counter was used as the detector. To minimize effects due to spatial divergence of the reflected beam a Soller-aperture (width=1 mm) was

mounted in front of the detector entrance slit. The resolution limit of the diffractometer was checked using a reference quartz sample and a Al_2O_3 (Corrund) powder. The Full-Width-Half-Maximum (FWHM) of all peaks was in the range of $0.045° - 0.07°$. Their was no significant angle dependence of the peak width; only a slight increase with decreasing peak intensity. Two-theta offsets were also checked using these standards.

Two scanning modes were used during this work, i.e. symmetric scanning and asymmetric scanning. Standard symmetric XRD Θ-2Θ scans give an integral picture of a thin film sample, since the intensity of the incident radiation is nearly homogeneous across the sample thickness. In order realize more surface sensitive scans asymmetric scans were performed where the incident beam is fixed at a very small angle Φ and only the detector is scanned. Figure 2.10 gives a schematic overview of the two modes.

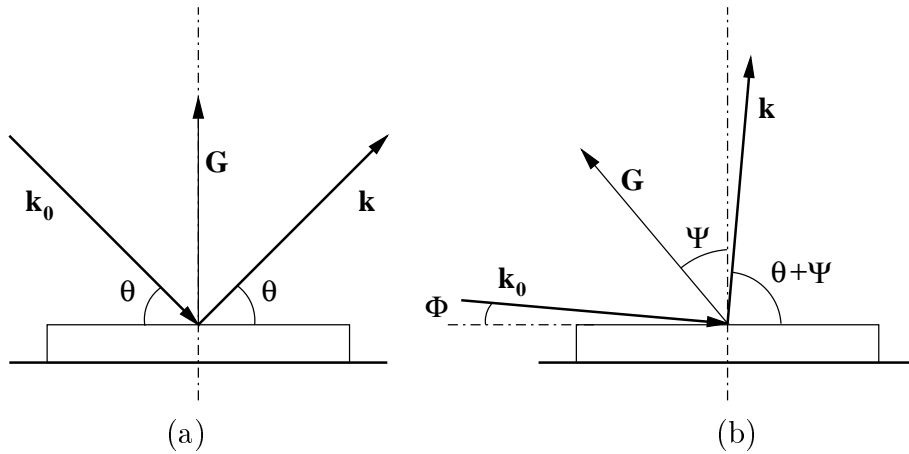The penetration depth of the incident X-ray intensity into a thin film, assuming an

Figure 2.10: Experimental geometry of the Bragg-Bretano method for X-ray diffraction; (a) symmetric mode, (b) asymmetric mode.

absorption coefficient of $\mu = 730\,\mathrm{cm^{-1}}$ (corresponds to $CuInS_2$), is plotted in Figure 2.11 for different angles of incidence of the primary beam. It can clearly be seen that for an incident angle of $\Phi = 5.0°$ the sampling volume accessible for XRD is of the order of $2\,\mu\mathrm{m}$ which is the typical thickness of samples investigated in this work. In the case of an angle of incidence of $\Phi = 0.5°$ the first $500\,\mathrm{nm}$ only will contribute to the measurement. Thus by varying Φ the surface sensitivity of the measurement can be influenced. This is particularly useful when analyzing bilayer structures of unknown stacking sequence. The change in the intensity ratio of reflections from the different layers with incident angle can be used to determine the relative location of the different layers. X-ray absorption in a thin film sample as a function of incident angle is also discussed in Appendix A.3.
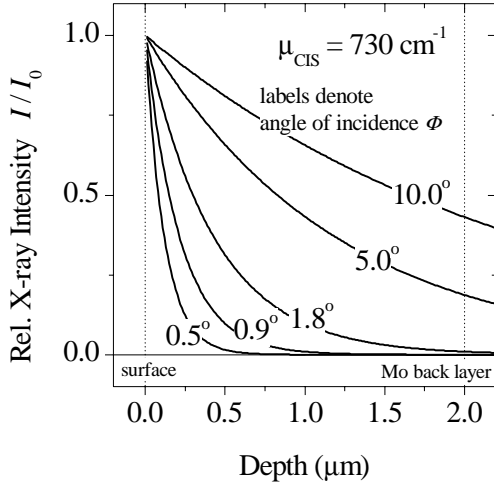
Figure 2.11: Calculated X-ray intensity versus sample depth for different angle of incidence of the primary beam. The assumed X-ray absorption coefficient of $\mu = 730\,\mathrm{cm}^{-1}$ corresponds to CuInS$_2$.

2.2.4 Calculation of XRD spectra

Calculated X-ray diffraction spectra for Cu(In$_{1-x}$Ga$_x$)S$_2$ thin films were employed in this work in order to evaluate measured XRD data. A script based on the software package *MATHEMATICA*$^{(\mathrm{TM})}$ [90] was written, so that effects of structural deviations and effects due to gradients in lattice constant could be simulated.

Structure factors were calculated from Equation (2.6). Values for the atomic scattering factors were interpolated form tabulated values taken from the International Tables of Crystallography [91]. Dispersion was accounted for by applying the correction factors of Cromer and Liberman [92]. Isotropic Debye-Waller temperature factors were taken from the crystal refinement of single crystals of CuInS$_2$ and CuGaS$_2$ by Abrahams and Bernstein [23]. On the basis of the structure factors peak intensities were calculated taking into account absorption of X-rays in the sample and the thin film geometry. All correction factors considered in the simulations are discussed in Appendix A.3. Calculated peak profiles were based on the Pearson-VII function according to Equation (2.10). The full width at half maximum parameter (FWHM) and the peak-shape parameter n were obtained from fits to experimental data of reference samples. All calculations were done for Cu-K$_{\alpha 1}$ and Cu-K$_{\alpha 2}$ radiation with an assumed intensity ratio of K$_{\alpha 2}$/K$_{\alpha 1}$ = 1/2. A list of the parameters used can be found in Appendix A.4.

To compute the XRD-spectrum for a layer with variable lattice constant along the depth profile, the layer was subdivided into laminae of constant lattice constants. The XRD spectrum was then obtained by summing up the reflected intensities of each lamina corrected for absorption of the incident and the scattered beam in the overlying layers. The minimum number of laminae required was determined empirically by recalculating the spectrum with increasing number of laminae until no detectable change in the calculated output, with respect to the experimental resolution limit of 0.01°, occurred.

2.2.4.1   X-ray structure factors of $CuInS_2$ and $CuGaS_2$

As shown in Section 2.2.3.1, Equation (2.6), the structure factor describes the coherent superposition of scattered waves originating from the individual atomic positions in the unit cell. Depending on the specific structure interference might be either constructive or destructive, hence not all reciprocal lattice vectors which satisfy Bragg's law will lead to a reflection in an experiment.

For a chalcopyrite structures such as $CuInS_2$ and $CuGaS_2$ the allowed reflections fall into one of three categories [93].
Group (i) reflections have $(h, k, l/2)$ all even or odd. These reflections correspond to the zincblende structure. A I-III-VI$_2$ compound with random occupation of the cation lattice site (sphalerite) would lead to group (i) reflections only. In most ternary chalcopyrites the tetragonal unit cell is distorted, i.e. $2c \neq a$. As a result the multiplicity of zincblende reflections with $h \neq l/2$ or $k \neq l/2$ is reduced and the singular zincblende reflection is split into a doublet, e.g. $(2, 0, 0)_{\text{zincblende}} \rightarrow (2, 0, 0)/(0, 0, 4)_{\text{chalcopyrite}}$.
Group (ii) reflections have indices given by (h, k) even and $(l/2)$ odd or vice versa. The structure factor of these reflections depends only on the anion scattering factor. If $u = 0.25$, i.e. no anion displacement, the structure factor vanishes.
Group (iii) reflections have indices given by (h) even and (k, l) odd or (k) even and (h, l) odd. The structure factor contains a cation term which arises from the difference in the cation scattering factors and, in case $u \neq 0.25$ also an anion term. These reflections are also called superlattice peaks.

A list of calculated F_{hkl} values for selected reflections of $CuInS_2$ and $CuGaS_2$ can be found in Table 2.1. The table also compares the calculated data to values reported by Jaffe and Zunger [8]. Their values are based on the Fourier transform of the calculated electronic charge densities, which were calculated self-consistently by means of a density-functional formalism. Both sets of data were calculated with the same set of lattice parameters given in [24] and listed in Table 1.1. The agreement is reasonably well, taking into account that the calculations of this work are based on tabulated atomic scattering factors for neutral atoms which do not account for changes in the electron density due to chemical bonding and lattice formation. For a $CuInS_2$ and $CuGaS_2$ film of $2.5\,\mu$m thickness the calculated XRD intensity spectra (Θ-2Θ scan, Bragg-Bretano geometry) are depicted in Figure 2.12.

Using the classification (i)–(iii) for chalcopyrite structure factors the following trends can be deduced.
Group (i) or zincblende like reflections are the most intense in the spectra. The (112) and the (024)/(020) lattice planes have the highest packing density and therefore the corresponding peaks dominate the spectra. Due to the lower atomic scattering factor for Ga compared to In, XRD reflections for $CuGaS_2$ are by one fifth weaker in intensity than the corresponding $CuInS_2$ reflections.
The effect of the tetragonal distortion of the chalcopyrite unit cell on the (024)/(220) group (i) reflections is demonstrated in Figure 2.13. The distortion c/a is greater than 2 in

Table 2.1: Comparison of calculated structure factors F_{hkl} in $e/$(primitive cell) of selective XRD reflections of $CuInS_2$ and $CuGaS_2$ from Ref. [8] and this work.

hkl	group	$CuGaS_2$ [8]	$CuGaS_2$ this work	$CuInS_2$ [8]	$CuInS_2$ this work
(112)	(i)	112.77	113.28	142.63	143.35
(200)	(i)	53.32	53.87	84.94	85.70
(004)	(i)	51.98	52.57	82.78	83.44
(204)	(i)	123.04	124.60	151.57	153.37
(220)	(i)	122.86	124.41	149.43	151.18
(116)	(i)	86.21	87.64	112.28	113.74
(312)	(i)	86.43	87.86	111.01	112.42
(224)	(i)	45.67	46.16	73.50	73.74
(008)	(i)	102.12	103.61	129.07	130.74
(400)	(i)	100.70	102.20	122.42	123.98
(202)	(ii)	1.09	1.06	2.14	2.23
(310)	(ii)	1.56	1.77	3.28	3.64
(402)	(ii)	2.98	3.04	6.11	6.19
(101)	(iii)	6.63	6.61	19.56	19.72
(103)	(iii)	1.75	1.84	29.38	29.51
(121)	(iii)	6.85	6.81	29.11	29.09
(123)	(iii)	8.13	7.95	19.31	19.15
(233)	(iii)	6.83	7.08	30.30	30.23

$CuInS_2$ and less than 2 in $CuGaS_2$. (Table 1.1). The values in the alloyed $Cu(In_{1-x}Ga_x)S_2$ system obey Vegard's law [25], i.e. they vary linearly with composition x (Figure 2.13 (a)). Figure 2.13 (b) shows calculated (024)/(220) reflections of a $Cu(In_{1-x}Ga_x)S_2$ thin film as a function of composition x. The doublet structure with an intensity ratio $I_{220}/I_{024} \approx 1/2$ can clearly be seen. Although, the anion displacement changes quite significantly between $CuInS_2$ and $CuGaS_2$ its influence on the structure factors of group (i) peaks is negligible. Since the tetragonal distortion arises from the ordered cation sublattice in the chalcopyrite structure the peak splitting serves as a good indicator for the degree of chalcopyrite cation ordering in a sample. At $x \approx 0.2$ where $c/a = 2.0$ the distortion vanishes and no peak splitting is observed.

In such a case chalcopyrite ordering can only be evaluated by analyzing the group (iii) peak intensities, which are determined by the difference in scattering factor at the different cation sites in the unit cell. In $CuGaS_2$ the structure factors of this group are rather small, i.e. below $10\,e/$cell (Table 2.1), since f_{Cu} almost equals f_{Ga}. As can be seen in Figure 2.12 only the (101) reflection at 18.0° can be expected to be above the detection limit. At higher 2θ values the superlattice of a $CuGaS_2$ thin film are very weak since the peak intensities are significantly reduced by the polarization and Lorentz-factors and in case of a thin film sample additionally by the reduced scattering volume. In $CuInS_2$ the situation is different as the large difference between f_{Cu} and f_{In} leads to much higher structure factors for group (iii) peaks. At least five superlattice peaks can be well resolved at the simulated
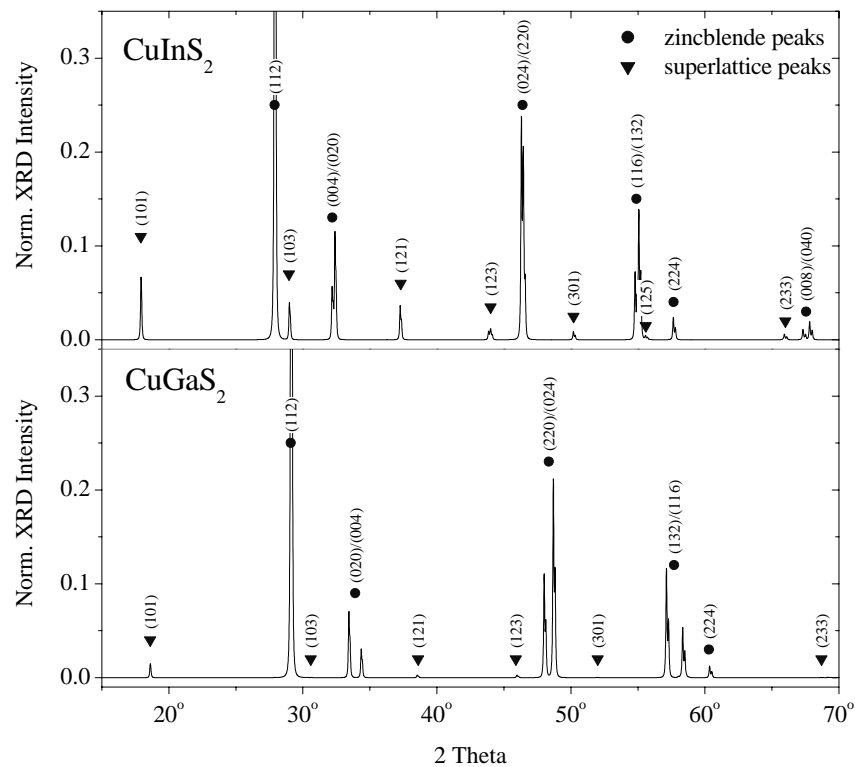
Figure 2.12: Calculated XRD spectra of $CuInS_2$ (upper plot) and $CuGaS_2$(lower plot). Intensities are plotted relative to the (112) reflection.

spectra of the $CuInS_2$ thin film in Figure 2.12. The influence of structural deviations from an ideal chalcopyrite unit cell onto the group (iii) reflections of a $CuInS_2$ thin film such as cation order/disorder transitions, deviations from molecularity, changes in the anion displacement u, and the isovalent substitution of In with Ga is discussed in Appendix A.1. Most of the group (ii) structure factors are well below 5 electrons/cell, which leads to reflections that are in general below the detection limit of a XRD-measurement at a powder sample. No group (ii) reflection was observed at samples of this work.
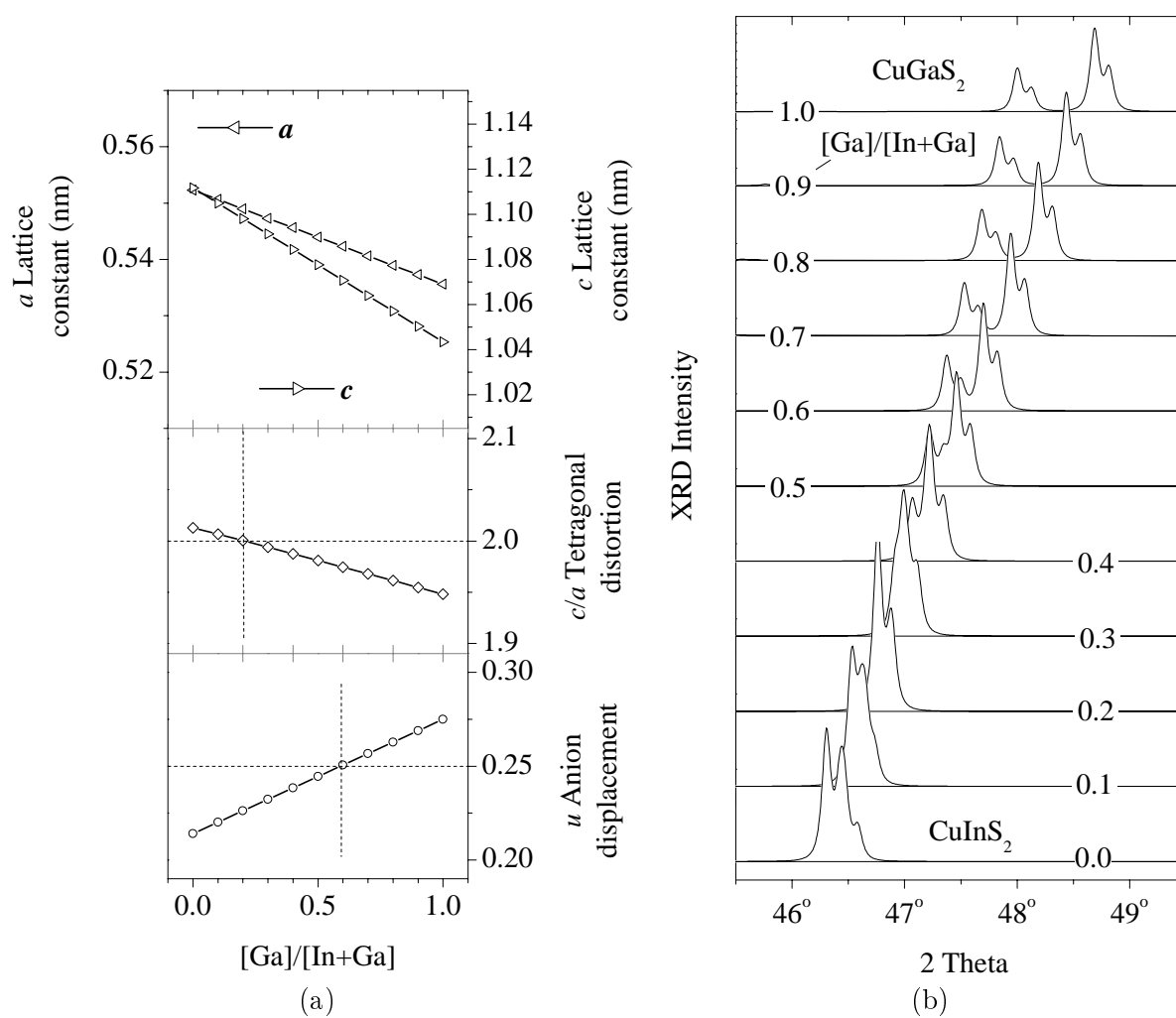
Figure 2.13: (a) Lattice constants, tetragonal distortion and anion displacement of the $Cu(In_{1-x}Ga_x)S_2$ alloy system as a function of x and (b) corresponding XRD-spectra of the $(024)/(220)$ doublet for Cu-$K_{\alpha 1}$ and Cu-$K_{\alpha 2}$ radiation. The characteristic peak splitting vanishes at $[Ga]/([In]+[Ga]) \approx 0.2$ where $c/a = 2.0$.